



A surfactant-assisted synthesis route for scalable preparation of high performance of $\text{LiFe}_{0.15}\text{Mn}_{0.85}\text{PO}_4/\text{C}$ cathode using bimetallic precursor

Xue Zhou ^a, Yuanfu Deng ^{a,b,*}, Lina Wan ^a, Xusong Qin ^b, Guohua Chen ^{b,c,*}

^a The Key Laboratory of Fuel Cell of Guangdong Province, School of Chemistry and Chemical Engineering, South China University of Technology, Guangzhou, China

^b Center for Green Products and Processing Technologies, Guangzhou HKUST Fok Ying Tung Research Institute, Guangzhou 511458, China

^c Department of Chemical and Biomolecular Engineering, The Hong Kong University of Science and Technology, Hong Kong, China



HIGHLIGHTS

- $\text{LiFe}_{0.15}\text{Mn}_{0.85}\text{PO}_4/\text{C}$ composite is prepared by a surfactant-assisted milling route.
- The $\text{LiFe}_{0.15}\text{Mn}_{0.85}\text{PO}_4/\text{C}$ composite exhibits excellent rate and cycle capability.
- Stable cycle properties are ascribed to uniform carbon-coated nanostructures.

ARTICLE INFO

Article history:

Received 26 January 2014

Received in revised form

19 March 2014

Accepted 11 April 2014

Available online 9 May 2014

Keywords:

Homogeneous precursor
Lithium iron–manganese phosphate
Surfactant-assisted route
Lithium ion battery
Rate performance

ABSTRACT

A uniform carbon coated $\text{LiFe}_{0.15}\text{Mn}_{0.85}\text{PO}_4$ (LFMP/C) cathode material is synthesized by a surfactant-assisted, highly reproducible and energy-saving solid state method using a bimetallic oxalate ($\text{Fe}_{0.15}\text{Mn}_{0.85}\text{C}_2\text{O}_4$) precursor. The obtained $\text{LiFe}_{0.15}\text{Mn}_{0.85}\text{PO}_4/\text{C}$ composite is characterized by X-ray diffraction (XRD), Raman spectrum, elemental analysis (EA), scanning electron microscopy (SEM), and transmission electron microscopy (TEM). The experimental results demonstrate that the oleic acid as a surfactant, for the scale preparation of LFMP, plays a critical role in controlling size of the obtained composite. The $\text{LiFe}_{0.15}\text{Mn}_{0.85}\text{PO}_4/\text{C}$ exhibits high specific capacity and good rate performance. It delivers initial discharge capacities of 156.5, 142.5, 129.0 and 103.0 mAh g^{-1} at 0.05, 0.1, 0.5 and 1C, respectively. Moreover, it shows good cycle stability at both room temperature (25 °C, 89% and 88% capacity retention after 250 and 500 cycles at 0.5 and 1C rates, respectively) and elevated temperature (55 °C, 80% capacity retention after 200 cycles at 0.5C rate). The significantly improved rate and cycling capability of the $\text{LiFe}_{0.15}\text{Mn}_{0.85}\text{PO}_4/\text{C}$ is attributed to the uniform carbon coating layer on the primary particles, the conductive network provided by the carbon between the $\text{LiMn}_{0.15}\text{Fe}_{0.85}\text{PO}_4/\text{C}$ particles and the sufficient pores formed in the $\text{LiFe}_{0.15}\text{Mn}_{0.85}\text{PO}_4/\text{C}$ aggregates.

© 2014 Elsevier B.V. All rights reserved.

1. Introduction

In recent years, phosphate-based cathode materials have attracted considerable attention as potential alternatives to commercial layered cathode materials for their superiorities on structural stability, cost effectiveness and environmental friendliness [1,2]. Among them, LiMnPO_4 is one of the most attractive materials due to its high theoretical specific capacity (170 mAh g^{-1}) and

suitable redox potential (4.1 V vs. Li/Li^+) [3]. However, its application in practical lithium ion batteries (LIBs) has been impeded by the low discharge capacity and the bad rate performance arising from its intrinsically low electric and ionic conductivity, and the poor capacity retention due to the dissolution of Mn during the cycling [3,4]. To compensate the above drawbacks of LiMnPO_4 , traditional approaches such as the control of the primary particle size [5–7], particle morphology [8–11] and carbon coating [12–17] have been investigated. Indeed, LiMnPO_4 particles of size ~ 50 nm have been obtained by different synthesis routes: solvothermal synthesis [5], Sol–gel plus ball milling [7], solid-state reaction in molten hydrocarbon [8], and spray pyrolysis plus ball milling [14,15]. The best result has been obtained by Choi et al. who

* Corresponding authors. The Key Laboratory of Fuel Cell of Guangdong Province, School of Chemistry and Chemical Engineering, South China University of Technology, Guangzhou, China. Tel./fax: +86 20 87112053.

E-mail addresses: chyfdeng@scut.edu.cn (Y. Deng), kechengh@ust.hk (G. Chen).

synthesized LiMnPO_4 nanoplates with a thickness of 50 nm that are assembled and grew into nanorods along the [010] direction in the (100) plane [9]. The capacity of 168 mAh g^{-1} at very low rate C/50 obtained in this case is close to the theoretical value. At faster rates, however, crucial for electric vehicles that require high power supplies, LiMnPO_4 still need to be improved. Many efforts made to obtain high performance LiMnPO_4/C composites, the capacities remain low. The capacities of $130\text{--}140 \text{ mAh g}^{-1}$ at rate C/10 can be obtained only if the particles are immersed in a huge quantity of carbon, typically 20 wt% [16] up to 30 wt% [14,15]. However, the large amount of carbon in the above materials may bring low tap density, which is an obvious disadvantage for cathode material.

Another important method for improving the cycling and rate performance of LiMnPO_4 or LiMnPO_4/C cathode materials has been investigated recently by Fe^{2+} ions doping [18–25]. For example, Martha and co-workers reported that $\text{LiFe}_{0.2}\text{Mn}_{0.8}\text{PO}_4$ nanoparticles (25–60 nm) with 10 wt% carbon coating showed good rate performance with an initial capacity of 93 mAh g^{-1} at 10C rate [18]. The large amount of carbon in this material may bring low tap density, which is an obvious disadvantage for cathode material. The $\text{LiMn}_{0.75}\text{Fe}_{0.25}\text{PO}_4$ nanorods/graphene [19] and the $\text{LiMn}_{0.5}\text{Fe}_{0.5}\text{PO}_4$ nanoplates [20] with good rate performance were obtained through two solvothermal route in 2011 and 2014, respectively. However, large amount of organic solvents were required in the solvothermal synthesis process which may result in severe environment pollution. As the consequence, the solvothermal route is not suitable for large-scale production. State-of-art $\text{LiFe}_{0.5}\text{Mn}_{0.5}\text{PO}_4/\text{C}$ [21] and $\text{LiFe}_{0.6}\text{Mn}_{0.4}\text{PO}_4/\text{C}$ [22] microspheres have been respectively synthesized by a co-precipitation route and a double carbon coating-spray drying method. Both of these two cathode materials showed high tap density, high specific capacity and rate performance at room temperature. However, the disadvantage of this method is the complex process for carbon coating. Besides, large of Fe substitution in the two samples is not enough to take the maximum benefit of the higher working potential with Mn. More recently, Ding et al. improved the rate performance (116 mAh g^{-1} at 5C-rate) and cycle stability (95% retention of initial capacity in 50 cycles at 0.5C-rate) of LiMnPO_4 by collective and cooperative strategies including Fe substitution, carbon coating, and the morphology-controlling [23]. However, the long cycling performance at room temperature and the electrochemical performance at elevated temperature, which is a critical parameter for the cathode material valuation, of the obtained cathode materials have not been reported.

An improvement for rate performance of LiMnPO_4 has also been obtained recently via a multi-composite synthesis process [28]. The core–shell structure $2/3\text{LiMnPO}_4@1/3\text{LiPO}_4/\text{C}$ composite shows much improvement rate performance (90 mAh g^{-1} at 1C-rate) than that of a powder of $\text{LiMn}_{2/3}\text{Fe}_{1/3}\text{PO}_4$ particles. More recently, $\text{C-LiFe}_x\text{Mn}_{1-x}\text{PO}_4\text{-LiFePO}_4$ composites with different x values ($0 \leq x \leq 0.5$) for improving the electrochemical performance of LiMnPO_4 have also been synthesized by other groups [29–31]. The multi-composite synthesis process has an effective strategy for improvement the electrochemical performance of LiMnPO_4 -based cathodes, however, the complex route was also hinder its practical application in large scale.

Simplicity of the synthesis process is important for commercializing LIBs. From this perspective, a solid state synthesis route for the preparation high performance LiMnPO_4 -based cathode material effectively is propitious to reach its industrialization [4]. For example, $\text{LiFe}_{0.5}\text{Mn}_{0.5}\text{PO}_4/\text{C}$ with a reversible capacity of 138 mAh g^{-1} at 0.1C-rate was obtained by rheological phase reaction using five respective raw materials [27]. These many starting precursors may bring inhomogeneous composition distribution of the final product in the practical application. Hu et al. prepared Fe

and Mg co-doped LiMnPO_4 with 14wt% of sucrose via a solid-state route with subsequent ball milling for 6 h [32]. The $\text{LiMn}_{0.9}\text{Fe}_{0.05}\text{Mg}_{0.05}\text{PO}_4$ sample, obtaining from 850°C , shows the initial discharge capacity of 121 mAh g^{-1} at 0.2C-rate. The high temperature for this process to increased electronic conductivity of the carbon film. Hong et al. prepared $\text{LiMn}_{1-x}\text{Fe}_x\text{PO}_4$ ($x = 0, 0.05, 0.1, 0.15$, and 0.2) with an appropriate amount of citric acid as the carbon source and subsequently employed planetary ball milling for about 3.5 days before the heat treatment [33]. The $\text{LiFe}_{0.2}\text{Mn}_{0.8}\text{PO}_4/\text{C}$ resulted in a specific capacity of 138 mAh g^{-1} at 0.1C-rate. The long time used for ball milling before the heat treatment would result in extra energy-wasting. Ran synthesized LiMnPO_4/C with 134 mAh g^{-1} at 0.1C-rate via polyvinyl pyrrolidone-assisted (PVP) solid state reaction [34] in 2013. This result shows that this method is an effective route for preparation of LiMnPO_4 -based materials. In addition, recent research results also demonstrated that PVP/Polymers have important role on controlling the particle size during preparation of the cathode materials [35,36]. In order to overcome the difficulties during the preparation high performance LMFP-based cathode materials via the traditional solid-state reaction, herein, a scalable and highly reproducible synthesis route was proposed to prepare homogenous carbon coated $\text{LiFe}_{0.15}\text{Mn}_{0.85}\text{PO}_4$ cathode material. The proposed synthesis route is based on oleic acid-assisted ball milling method, in the first time, using a homogeneous bimetallic oxalate ($\text{Fe}_{0.15}\text{Mn}_{0.85}\text{C}_2\text{O}_4$) compound, sp^2 -dominated carbon source (phenolic resin) and LiH_2PO_4 as raw materials. Detailed characterizations on the physical and electrochemical properties of the as-synthesized composite material had been conducted. Interesting results were obtained as discussed subsequently.

2. Experimental

2.1. Material preparation

Homogenous bimetallic metal oxalate ($\text{Fe}_{0.15}\text{Mn}_{0.85}\text{C}_2\text{O}_4 \cdot 2\text{H}_2\text{O}$) was prepared by the co-precipitation method. $\text{MnSO}_4 \cdot 4\text{H}_2\text{O}$ (3.7920 g, AR, Aladdin Chemical Agents Co. Ltd) and $\text{FeSO}_4 \cdot 7\text{H}_2\text{O}$ (0.8341 g, AR, Aladdin Chemical Agents Co. Ltd) were dissolved in water successively to prepare 20 mL of bimetallic sulfate solution (0.5 M in MnSO_4 and FeSO_4 , respectively). After that, 41 mL of sodium oxalate solution (0.5 M) was added into the bimetallic sulfate solution quickly under continuous stirring and a N_2 atmosphere. The stirring was maintained for 15 min. Bright yellow particles were then collected via filtration, washed with distilled water three times, and dried in a vacuum oven at 60°C for 12 h to obtain the $\text{Fe}_{0.15}\text{Mn}_{0.85}\text{C}_2\text{O}_4 \cdot 2\text{H}_2\text{O}$ product.

The synthesis of $\text{LiFe}_{0.15}\text{Mn}_{0.85}\text{PO}_4/\text{C}$ was carried out as follows: stoichiometric amounts of LiH_2PO_4 (1.0393 g, AR, Aladdin Chemical Agents Co. Ltd), $\text{Fe}_{0.15}\text{Mn}_{0.85}\text{C}_2\text{O}_4 \cdot 2\text{H}_2\text{O}$ (1.7912 g), phenolic resin (0.0787 g, AR, Shanghai Chemical Agents Co. Ltd) and oleic acid (1.5 g) were dispersed in ethanol (AR, Guangzhou Chemical agents Co. Ltd) and then ball-milled for 4 h at 400 RPM. The mixtures were dried under vacuum for 10 h at 80°C and then transferred to a tube furnace for calcination at 250°C for 2 h under an Ar atmosphere. After that, the calcination temperature was raised to 600°C and kept for 10 h to obtain a uniform carbon coating $\text{LiFe}_{0.15}\text{Mn}_{0.85}\text{PO}_4$ (LFMP-S1). Similarly, another $\text{LiFe}_{0.15}\text{Mn}_{0.85}\text{PO}_4$ (LFMP-S2) sample without adding oleic acid was also synthesized for comparison in the same procedures.

2.2. Materials characterization

The crystalline structure and particle morphology of $\text{LiFe}_{0.15}\text{Mn}_{0.85}\text{PO}_4/\text{C}$ samples were characterized by X-ray diffraction (XRD)

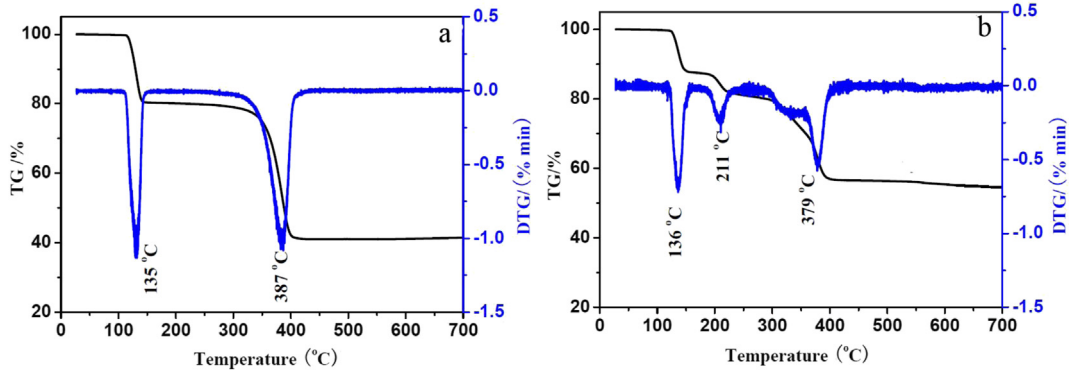


Fig. 1. TG and DTG curves of (a) $\text{Fe}_{0.15}\text{Mn}_{0.85}\text{C}_2\text{O}_4 \cdot 2\text{H}_2\text{O}$ and (b) $\text{LiFe}_{0.15}\text{Mn}_{0.85}\text{PO}_4/\text{C}$ mixed precursors.

(Bruker D8 ADVANCE, Cu $\text{K}\alpha$ radiation, $\lambda = 1.5406 \text{ \AA}$), scanning electron microscopy (SEM, JEOL 6300F) and transmission electron microscopy (TEM, PHILIPS TECNAI F30). Raman spectrum was obtained with a Bio-Rad FTS6000 Raman spectroscopy with a 532 nm blue laser beam. Fourier transform infrared (FT-IR) spectrum was recorded with KBr pellets using a Bruker R 200-L spectrophotometer. Therogravimetric (TG) analysis was carried out using a Netzsch STA 409EP thermal analyzer with a heating rate of $5 \text{ }^{\circ}\text{C min}^{-1}$ in N_2 to determine the sintering temperature. The carbon content of the $\text{LiFe}_{0.15}\text{Mn}_{0.85}\text{PO}_4/\text{C}$ was determined by an elemental analyzer (Vario EL III, Elemental Analysensystem).

2.3. Electrochemical measurements

To evaluate the electrochemical performance of the obtained samples, electrodes consisting of 80 wt% $\text{LiFe}_{0.15}\text{Mn}_{0.85}\text{PO}_4/\text{C}$, 10 wt% acetylene black and 10 wt% polyvinylidene fluoride (PVDF) were prepared on alumina foil by a tape-casting technique. Coin cells (CR2025) were assembled using the prepared $\text{LiFe}_{0.15}\text{Mn}_{0.85}\text{PO}_4/\text{C}$ electrode as cathode, lithium metal foil as anode, 1.0 M LiPF_6 solution in ethylene carbonate/ethylene methyl carbonate (EC:EMC = 1:1 v/v) as electrolyte and Celgard 2400 as separator in an Ar-filled glove box (MBRAUN LAB MASTER130). The fabricated cells were cycled in the voltage range between 2.0 and 4.5 V vs. Li/Li^+ at different current rates on a multichannel battery test system (NEWARE CT-3008W). The cyclic voltammetric (CV) measurement was performed on an electrochemical workstation (AUTOLAB PGSTAT 101) at a scan rate of 0.1 mV s^{-1} in the range of 2.0–4.5 V vs. Li/Li^+ . The electrochemical impedance spectroscopy (EIS) data of the electrodes were acquired at room temperature using a Versastat 3 electrochemical workstation (Princeton Applied Research) before cycling, at a discharge state in the frequency ranging from 100 kHz to 10 mHz by imposing an alternate current with an amplitude of 10 mV on the electrode. The specific capacity in the paper is based on the mass of the $\text{LiFe}_{0.15}\text{Mn}_{0.85}\text{PO}_4/\text{C}$ composite.

3. Results and discussion

The TG/DTG curves of the $\text{Fe}_{0.15}\text{Mn}_{0.85}\text{C}_2\text{O}_4 \cdot 2\text{H}_2\text{O}$ precursor and the ball milling mixture of $\text{Fe}_{0.15}\text{Mn}_{0.85}\text{C}_2\text{O}_4 \cdot 2\text{H}_2\text{O}$, LiH_2PO_4 , phenolic resin and oleic acid at the heating rate of $5 \text{ }^{\circ}\text{C min}^{-1}$ from room temperature to 800 °C were shown in Fig. 1a and b, respectively. TG analysis of the $\text{Fe}_{0.15}\text{Mn}_{0.85}\text{C}_2\text{O}_4 \cdot 2\text{H}_2\text{O}$ precursor revealed that the compound decomposes in two basic steps to produce the final bimetallic oxide through heating in N_2 at approximately 420 °C. In the first stage, a 20.1% mass loss (calculated value: 20.1%) was found when heated from room temperature to 180 °C with a heat absorption peak observed at 135 °C, which is likely caused by

the elimination of the two water molecules. The subsequent thermal decomposition of this precursor occurs in the temperature range of 180–450 °C with an abrupt mass loss (39.2%), which can be attributed to the removal of the carbon monoxide and carbon dioxide molecules. This corresponds to a strong heat peak at 387 °C. There is a total mass loss of 59.5% during the pyrolysis of the $\text{Fe}_{0.15}\text{Mn}_{0.85}\text{C}_2\text{O}_4 \cdot 2\text{H}_2\text{O}$ precursor when it is heated to 450 °C. This value is in good agreement with the calculated mass loss of 60.3% that is required for the conversion of the bimetallic oxalate precursor into its corresponding bimetallic oxide ($\text{Fe}_{0.15}\text{Mn}_{0.85}\text{O}$) at 450 °C. Compared with single $\text{Fe}_{0.15}\text{Mn}_{0.85}\text{C}_2\text{O}_4 \cdot 2\text{H}_2\text{O}$ precursor, the thermal decomposition of the mixed precursors occurred in three well-defined steps, which were at 136, 21 and 379 °C, respectively. The first weight loss with a heat absorption peak at about 136 °C is attributed to the dehydration of the $\text{Fe}_{0.15}\text{Mn}_{0.85}\text{C}_2\text{O}_4 \cdot 2\text{H}_2\text{O}$ precursor, as discussed previously. A 12.2% mass loss (calculated value: 12.4%) from room temperature to 180 °C was observed. Another small weight loss between 180 and 230 °C may be corresponding to the initial decomposition of LiH_2PO_4 , forming lithium metaphosphate (LiPO_3). The third weight loss from 230 to 450 °C with a strong heat absorption peak at 379 °C corresponds to the decomposition of the $\text{Fe}_{0.15}\text{Mn}_{0.85}\text{C}_2\text{O}_4$ and phenolic resin, and the reaction of LiPO_3 and the bimetallic oxide ($\text{Fe}_{0.15}\text{Mn}_{0.85}\text{O}$) to form the final $\text{LiFe}_{0.15}\text{Mn}_{0.85}\text{PO}_4/\text{C}$ composite. No weight loss can be observed after 600 °C. The total mass loss (44.6%) is in good agreement with the calculated value of 44.2% based on 3.95% carbon content in the sample (The carbon content was determined by elemental analysis).

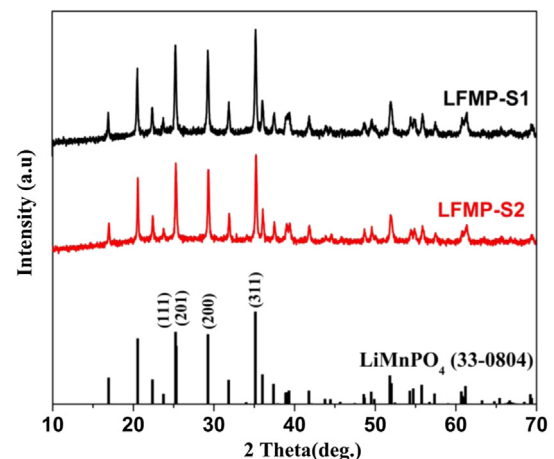


Fig. 2. (a) XRD patterns of the two $\text{LiFe}_{0.15}\text{Mn}_{0.85}\text{PO}_4/\text{C}$ composites and the standard LiMnPO_4 .

Fig. 2 shows XRD patterns of the two $\text{LiFe}_{0.15}\text{Mn}_{0.85}\text{PO}_4/\text{C}$ samples obtained from the same procedure with/without oleic acid. The two samples are pure olivine-type LiMnPO_4 pnm space group (JCPDS card no. 33-0804). The diffraction peaks of the two samples slightly shifted to higher degree due to the smaller ionic radii of Fe^{2+} . No peak of residual carbon was observed, which may be attributed to the low content and amorphous structure of carbon coating layer. The lattice parameters for LFMP-S1 were $a = 6.100$ (1) Å, $b = 10.447$ (3) Å, $c = 4.739$ (2) Å and $V = 302.02$ Å³, which is based on the calculation using MDI Jade 5.0 software. These values are consistent with the previously reported results [26,27] and LFMP-S2 [$a = 6.102$ (1) Å, $b = 10.448$ (1) Å, $c = 4.745$ (1) and $V = 302.54$ Å³]. The crystallite sizes of LFMP-S1 are $59.7 \times 87.3 \times 78.8$ nm, which was calculated using the Debye–Scherrer formula [$D = K\lambda/(\beta \cos \theta)$; where K is the Scherrer constant (close to 0.9), λ is the X-ray wavelength of $\text{Cu K}\alpha$ (0.154178 nm), β is the full width at half-maximum (FWHM) intensity of the prominent (111), (211) and (311) reflections in radian, and θ is the Bragg diffraction angle [37]. The crystallite size for LFMP-S2 is not calculated using the Debye–Scherrer formula because the particle size of this sample (>100 nm) is out of the calculation range.

Fig. 3 presents SEM images of the LFMP-1 and LFMP-2. The images show that both samples were composed of agglomerated nanoparticles, however, the particle size of LFMP-S1 is smaller than that of LFMP-S2. In addition, the particles of LFMP-S1 are more homogeneous. These results demonstrated that the oleic acid, acting as a surface-capping ligand of precursors with its carboxylic group, has important role for preventing the particles agglomeration by steric hindrance during high-energy ball milling [8]. As illustrated in **Fig. 3c**, the primary LFMP-S1 particles were mainly around 100 nm in size, which is in agreement with the calculation result based on the calculation result from the XRD pattern.

To examine the detail physical characters of the $\text{LiFe}_{0.15}\text{Mn}_{0.85}\text{PO}_4/\text{C}$ composites, LFMP-S1 was chose for further investigation. **Fig. 4a** displays the FT-IR spectrum of the LFMP-S1 composite in the 1300–400 cm⁻¹ corresponding to the stretching mode of PO_4^{3-} anion. The bands at 1140, 1094 and 1056 cm⁻¹ are

attributed to the asymmetric stretching mode (v_3), while the bands at 987 and 638 cm⁻¹ are ascribed to symmetric stretching mode (v_1) and asymmetric bending mode (v_4), respectively. The four bands at 576, 559, 505 and 470 cm⁻¹ correspond to the bending modes (v_2 and v_4) [26,38]. It is worthwhile noting that the band of bending mode v_1 which indicates the deformation of P–O, is in the range of that for LiFePO_4 (979 cm⁻¹ [39]) and LiMnPO_4 (989 cm⁻¹ [40]), revealing the homogenous distribution of iron and manganese in the $\text{LiFe}_{0.15}\text{Mn}_{0.85}\text{PO}_4$ solid solution. This observation is not in agreement with the recently reported result, in which the respective band positively shifted comparing with that for LiFePO_4 and LiMnPO_4 [26]. A TEM image in **Fig. 4b** shows the LFMP-S1 particles is in olive shape with particle size of about 100 nm length. Clear atomic lattice of the sample could be found in **Fig. 4c**, revealing a good crystallinity of the $\text{LiFe}_{0.15}\text{Mn}_{0.85}\text{PO}_4$ particle. An amorphous phase of carbon layer with a thickness of around 3 nm covered uniformly on the surface of primary particles was also observed in HTEM image (**Fig. 4c**). This result demonstrates that the dissolution of phenolic resin in ethanol is critical for the uniform distribution of carbon coating layer on the surface of $\text{LiFe}_{0.15}\text{Mn}_{0.85}\text{PO}_4$. The uniform distribution of carbon on the surface of primary $\text{LiFe}_{0.15}\text{Mn}_{0.85}\text{PO}_4$ particles was also demonstrated by the Raman spectrum of the LFMP-1 sample (**Fig. 4d**). As seen from **Fig. 3d**, the Raman signals of the $\text{LiFe}_{0.15}\text{Mn}_{0.85}\text{PO}_4/\text{C}$ displayed two strong and broad peaks at 1340 and 1590 cm⁻¹, attributing to the D band (disordered carbon) and G band (graphite) for amorphous carbon, respectively [9,41,42]. Only a small peak of the LFMP-S1 composite can be distinguished in the range of 600–1000 cm⁻¹ which corresponds to the character of PO_4^{3-} anion. These results are reasonable since the interaction between the PO_4^{3-} anion with the Raman laser was concealed by the uniform distribution of the carbon coating layer on the surface of the primary $\text{LiFe}_{0.15}\text{Mn}_{0.85}\text{PO}_4$ particles [43]. One may notice that some carbons were also distributed between the carbon-coated $\text{LiFe}_{0.15}\text{Mn}_{0.85}\text{PO}_4$ particles (**Fig. 4b**). The carbon could act as an effective conductive network between the $\text{LiFe}_{0.15}\text{Mn}_{0.85}\text{PO}_4/\text{C}$ particles, making a good conductivity of the composite. Furthermore, many pores within the

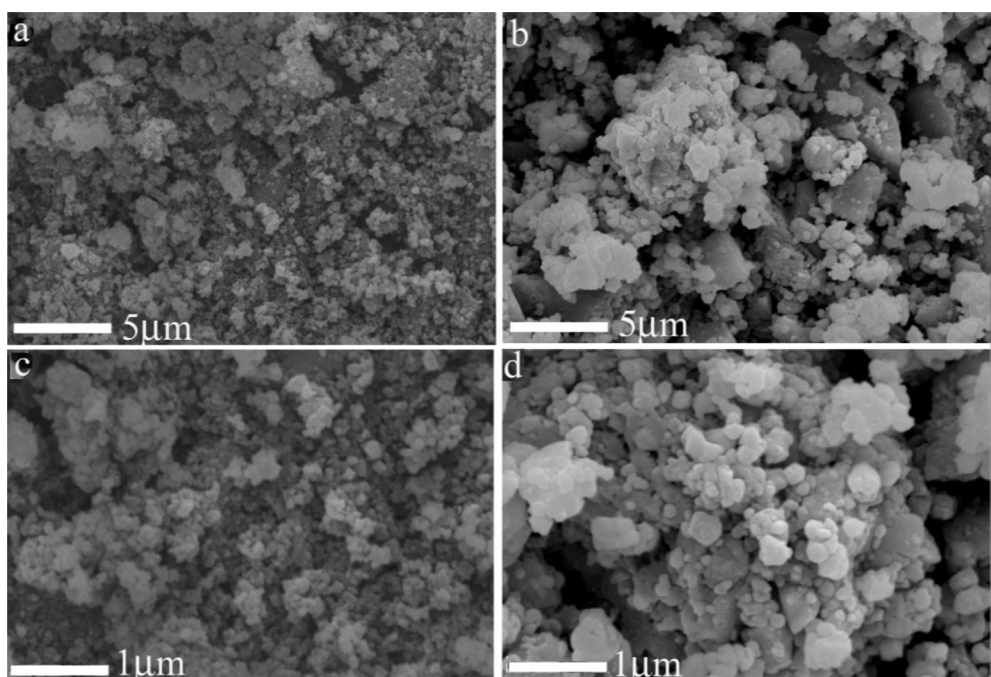


Fig. 3. SEM images: (a) and (c) for LFMP-S1 composite, and (b, d) for LFMP-S2 composite.

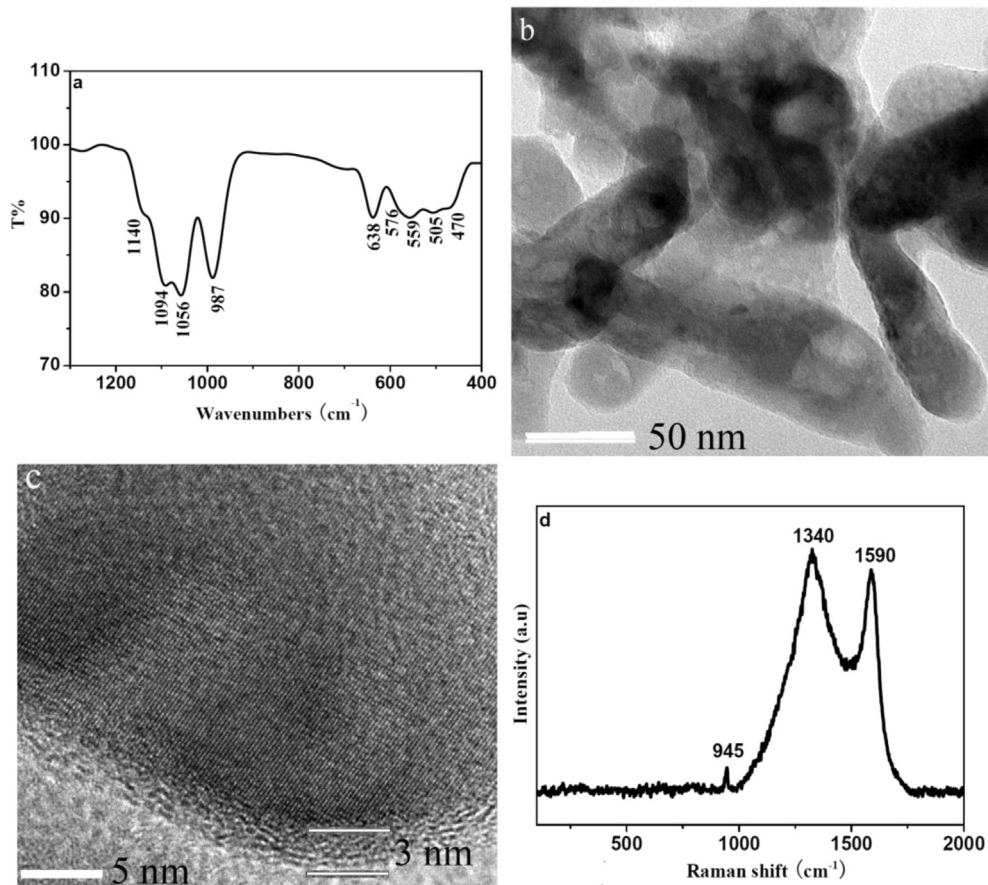


Fig. 4. (a) IR spectrum, (b) TEM image, (c) HTEM and (d) Raman spectrum of the LFMP-S1 composite.

$\text{LiFe}_{0.15}\text{Mn}_{0.85}\text{PO}_4/\text{C}$ particles and their micro-sized aggregates could be found in the SEM and TEM images (Figs. 3d and 4b), which favor fast Li^+ intercalation/deintercalation kinetics by allowing electrolyte insertion through the nanoparticles. The presence of uniform carbon coating layer, the conductive carbon network and the pores in the $\text{LiFe}_{0.15}\text{Mn}_{0.85}\text{PO}_4/\text{C}$ composite have synergistic effects on facilitating good transport of electrons and Li^+ from the poorly conducting $\text{LiFe}_{0.15}\text{Mn}_{0.85}\text{PO}_4$, improving effectively its specific discharge capacity and rate performance [16,44].

The electrochemical properties of the two $\text{LiFe}_{0.5}\text{Mn}_{0.5}\text{PO}_4/\text{C}$ composites as cathode materials for LIBs were investigated. Fig. 5a presents the first charge/discharge curves of the two

$\text{LiFe}_{0.15}\text{Mn}_{0.85}\text{PO}_4/\text{C}$ composites. The cells were charged to 4.5 V in a constant current-constant voltage mode at 0.05C ($1\text{C} = 170 \text{ mA g}^{-1}$) and discharge to 2.0 V at 0.05C rate (25°C). Both of the two samples exhibited two plateaus at 4.1 V and 3.5 V related to the $\text{Mn}^{3+}/\text{Mn}^{2+}$ and the $\text{Fe}^{3+}/\text{Fe}^{2+}$ redox couples [21,27]. At a low rate of 0.05C, the LFMP-S1 delivered a discharge capacity of 156.7 mAh g^{-1} . However, the LFMP-S2 only showed a discharge capacity of 135.1 mAh g^{-1} . In comparison with the LFMP-S2 electrode, the LFMP-S1 delivered much higher discharge capacity, which is attributed to a smaller particle size of LFMP-S1. To further understand the detail electrochemical performance of the LFMP-S1 with high discharge capacity, other electrochemical tests such as rate and cyclic performance,

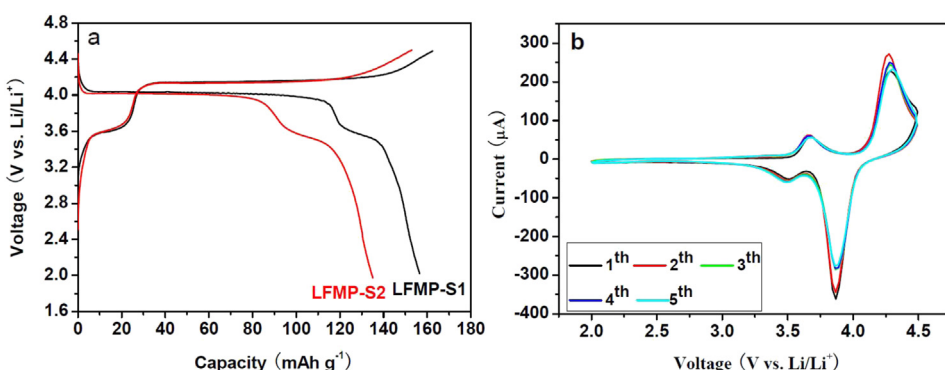


Fig. 5. (a) Charge–discharge curves at 0.05C ($1\text{C} = 170 \text{ mA g}^{-1}$) and (b) cyclic voltammograms at a scan rate of 0.1 mV s^{-1} of the LFMP-S1 composite.

CVs measurements and EIS were done. Fig. 5b displayed the CVs results of LFMP-S1, which showed oxidation and reduction peaks for $\text{Fe}^{2+}/\text{Fe}^{3+}$ and $\text{Mn}^{2+}/\text{Mn}^{3+}$, respectively. During the anodic (charge) sweep, two peaks appear at 3.67 and 4.25 V were attributed to the oxidation of Fe^{2+} to Fe^{3+} and $\text{Mn}^{2+}/\text{Mn}^{3+}$ respectively. Consequent cathodic (discharge) sweep reduces Mn^{3+} to Mn^{2+} at 3.90 V, followed by the reduction of Fe^{3+} to Fe^{2+} occurring at 3.50 V. These two couple oxidation/reduction peaks are well consistent with those in the charge/discharge curves listed in Fig. 4a. The voltage differences between the oxidation and reduction peaks of the CVs are 0.17 V for $\text{Fe}^{2+}/\text{Fe}^{3+}$ and 0.35 V for $\text{Mn}^{2+}/\text{Mn}^{3+}$, respectively. These results indicated that the partial incorporation of Fe into LiMnPO_4 facilitated the Li^+ diffusion in the structure by lowering the Li^+ diffusion barrier [21,44]. This was also demonstrated the low discharge capacity and large polarization of the as-prepared LiMnPO_4/C material using the same method (Figs. S1 and S2). The anodic and cathodic peak current was found to be stable after 4 cycles, which suggested that this electrode is high reversibility via an activation process.

The rate performance of the LFMP-S1 composite was investigated. As shown in Fig. 6a, it delivered average reversible specific capacities of 142.5, 136.0, 128.5, 104.0, 81.0 and 51.0 mAh g^{-1} at 0.1, 0.2, 0.5, 1, 2 and 5C rates, respectively. The average reversible specific capacities are higher than or comparable to the reported state-of-the-art $\text{LiMn}_{1-x}\text{Fe}_x\text{PO}_4$ -based materials [24,27,31–33,45,46]. It is quite impressed that even after charging/discharging at high current densities, the reversible specific capacity could still be recovered to 143.0 mAh g^{-1} when the current density was reduced to 0.1C. This clearly demonstrates the excellent current rate tolerance capability of the LFMP-S1 sample, comparing to the LiMnPO_4/C material (Fig. S1). Fig. 6b shows the discharge curves of the $\text{LiFe}_{0.15}\text{Mn}_{0.85}\text{PO}_4/\text{C}$ electrode obtained at different discharge current densities. The profiles at low charge/discharge rate (0.1C) clearly show two distinguished plateaus located at about 4.0 and 3.5 V versus Li/Li^+ . When the charge–discharge rate was increased to 5C, separation of the two discharge plateaus gradually became blurred and the plateau voltages shifted to lower values due to the increased cell polarization at very high current density. This phenomenon was also observed in other cathode materials such as LiMn_2O_4 [47]. Compared to the previous reports [24,27,31–33,45,46,48], the LFMP-S1 composite synthesized in the present study shows a comparable/higher specific discharge capacity at high discharge voltages (>3.5 V) when it is cycled at 0.5 and 1C rates, indicating that higher or comparable energy density could be achieved in these charge/discharge rates.

The cycle performances of the as-obtained LFMP-S1 sample at different current densities (0.1, 0.5 and 1C) charge/discharge are respectively shown in Fig. 7a and b. The corresponding charge/

discharge curves of selected cycles at 1C rate were also displayed in Fig. 7c and d, respectively. The LFMP-S1 sample showed initial capacities of 128.5 and 103.0 mAh g^{-1} at 0.5 and 1C, respectively. The capacity retention capability was 89% of 0.5C after 250 cycles and 88% of 1C after 500 cycles. This good capacity retention capability is compared to the state-of-art $\text{LiFe}_{1-x}\text{Mn}_x\text{PO}_4$ -based cathode materials [24,27,45,46,48]. Comparing the charge/discharge curves shown in Figs. 5a and 6b, one may notice that the discharge voltage plateau at ~4.0 V corresponding to $\text{Mn}^{2+}/\text{Mn}^{3+}$ redox reaction becomes shorter with current density increased. However, the discharge voltage plateau at 3.5 V which corresponds to $\text{Fe}^{2+}/\text{Fe}^{3+}$ redox reaction was almost the same. This fact suggested that the greater polarization appeared to $\text{Mn}^{2+}/\text{Mn}^{3+}$ rather than $\text{Fe}^{2+}/\text{Fe}^{3+}$ with charge/discharge current density increasing. Furthermore, the discharge capacity loss occurred mainly at above 3.5 V with increased current density and cycle number, which may also be attributed to the large polarization of the oxidation/reduction of $\text{Mn}^{2+}/\text{Mn}^{3+}$. The good capacity retention capability at different rates (The specific discharge capacity of LFMP-S1 at 0.1C rate was 143 mAh g^{-1} with 96.5% capacity retention, as shown in Fig. S3) of the $\text{LiFe}_{0.15}\text{Mn}_{0.85}\text{PO}_4/\text{C}$ material synthesized in the present study is due to the uniform distribution of a thin carbon coating layer on the surface of primary $\text{LiFe}_{0.15}\text{Mn}_{0.85}\text{PO}_4$ particles (as demonstrated by the TEM image and Raman spectrum), which plays a key role in suppressing the surface reactivity between the charged electrode and the electrolyte and decreasing the Mn dissolution [21]. Moreover, the capacity was still as high at 90 mAh g^{-1} even after 500 discharge–charge cycles at 1C (Fig. 6a), with 89% of capacity retention, suggesting the excellent cycling stability of the $\text{LiFe}_{0.15}\text{Mn}_{0.85}\text{PO}_4/\text{C}$ composite at high rate. The high capacities and excellent cycling stability imply that the $\text{LiFe}_{0.15}\text{Mn}_{0.85}\text{PO}_4/\text{C}$ composite could be a promising cathode material for high energy and power density LIBs.

To evaluate the cycle performance at elevated temperature, the as-prepared LFMP-S1 electrode was cycled at 0.5C-rate and 55 °C. As shown in Fig. 8a, this cathode material displayed an initial specific discharge capacity of 145.0 mAh g^{-1} , with 81% capacity retention capability after 200 cycles. In comparison with the charge/discharge curves at the same current density and different temperatures (25 and 55 °C, as shown in Figs. 7c and 8b, respectively), it was found that the increased discharge capacity appeared mainly in the 4.0 V region at high temperature. This observation shows that the specific discharge capacity of the $\text{LiMn}_{1-x}\text{Fe}_x\text{PO}_4$ -based materials can be improved at elevated temperature because of the faster Li^+ diffusion induced by the elevated temperature. Similar experimental results were also reported in literature [21,26]. To the best of our knowledge, it is a good example offering extended cycle life and good capacity retention capability at 0.5C-

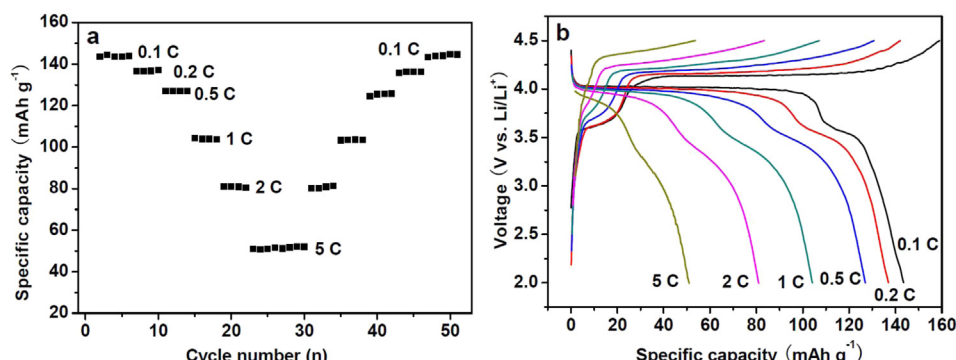


Fig. 6. (a) Rate performance at different C-rates and (b) charge–discharge curves of different C-rates of the LFMP-S1 composite.

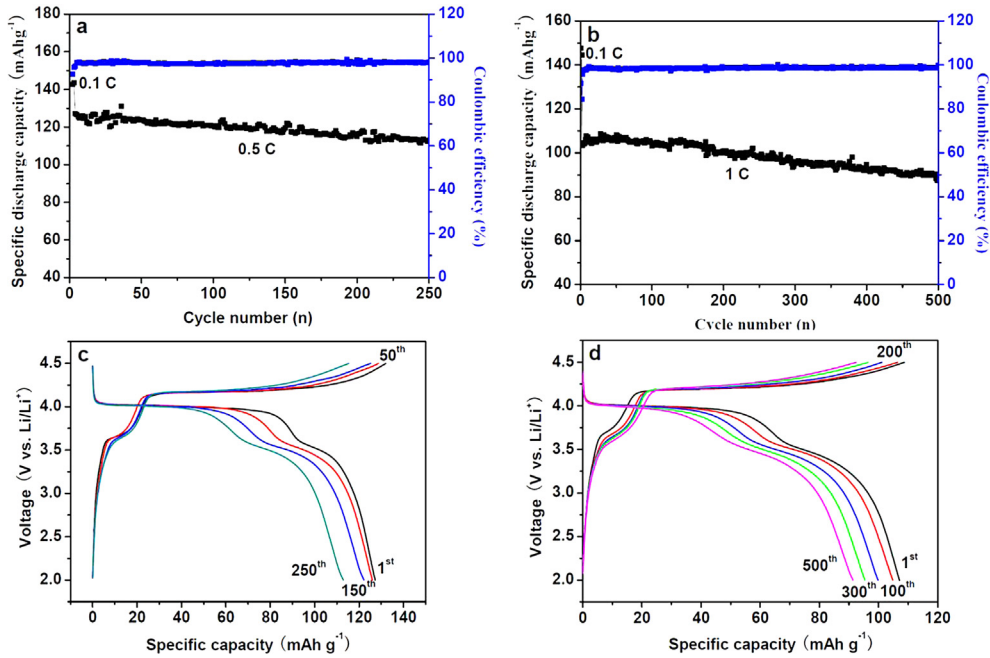


Fig. 7. (a) Cycling performance at 0.5C, (b) 1C rate, (c) charge–discharge curves of selective cycles at 0.5C and (d) 1C rate of the LFMP-S1 composite.

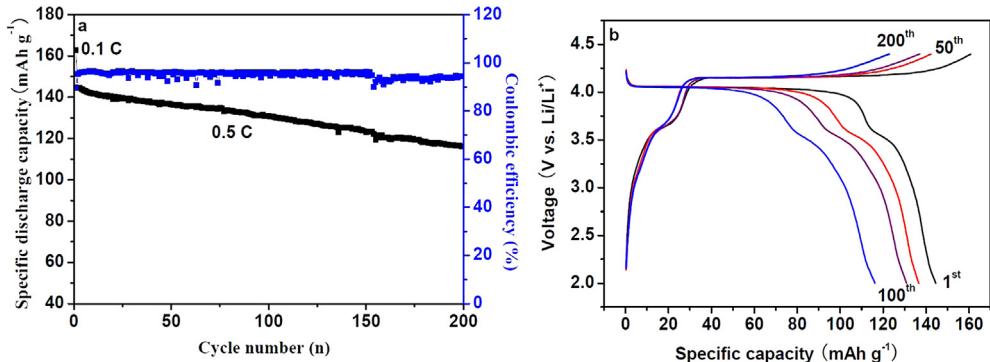


Fig. 8. (a) Cycling performance at 0.5C rate and 55 °C and (b) charge–discharge curves of the selective cycles at 0.5C rate and 55 °C of the LFMP-S1 composite.

rate and 55 °C for LiFe_{0.15}Mn_{0.85}PO₄/C cathode material. The good cycling performance at elevated temperature, a critical parameter for the cathode material valuation, of the as-prepared cathode material may also demonstrate that the LFMP-S1 composite is a promising cathode material.

To further understand the electrochemical performance of the two LiFe_{0.15}Mn_{0.85}PO₄/C samples synthesized with/without oleic acid as a surfactant, EIS was measured. Fig. 9 shows the EIS spectra of LFMP-S1 and LFMP-S2 electrodes. The two EIS spectra both consist of a very small intercept at high frequency, a depressed semicircle at high-to-medium frequency and an inclined line at low frequency. The small intercept is assigned to the solution resistance of the cell; the depressed semicircle corresponds to the charge-transfer resistance at electrode/electrolyte interface and the double-layer capacitance between the electrolyte and cathode; and the inclined line is attributed to a Warburg impedance related to the diffusion of lithium ions within the electrode [49]. The lower the charge-transfer resistance, the higher the electrochemical performances are [50]. A smaller diameter for the depressed semicircle means a lower charge-transfer resistance. As shown in Fig. 9, the LFMP-S1 electrode displays a lower charge-transfer

resistance than that of the LFMP-S2 sample, which indicates that the LFMP-S1 electrode holds faster charge transfer during charge/discharge, resulting in higher capacities and rate performance. The lower charge-transfer resistance and higher capacity of LFMP-S1

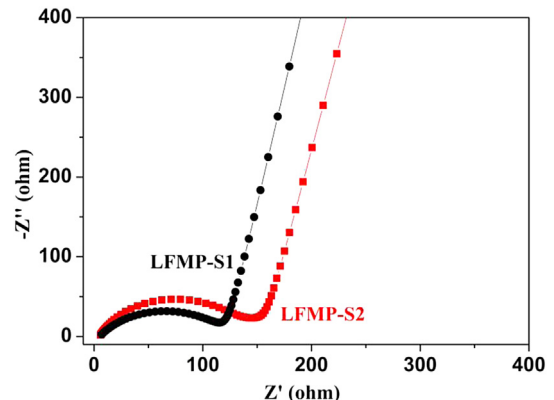


Fig. 9. EIS plots of the LFMP-S1 composite recorded in the fresh cells.

sample were attributed to the synergistic effect of Fe-doping and its smaller particle size, which could substantially improve electrochemical kinetics of lithium ion extraction/insertion.

4. Conclusions

In conclusion, $\text{LiFe}_{0.15}\text{Mn}_{0.85}\text{PO}_4/\text{C}$ cathode material with homogenous particle size distribution was successfully prepared via a facile, scalable and surfactant-assisted high-energy ball milling route, using the homogenous bimetallic oxalate, LiH_2PO_4 precursors and sp^2 -dominated carbon source. The electrochemical performance of LiMnPO_4 -based cathode material was highly dependent on the Fe-substituted and particle size. The as-prepared LFMP-S1 sample displayed high specific discharge capacity, good rate performance and excellent cycle performance at room and elevated temperature. The satisfactory electrochemical performance of the obtained LFMP-S1 composite could be attributed to the presence of a uniform carbon coating layer on the primary particles, an effective conduct network provided by the presence of carbon between the $\text{LiFe}_{0.15}\text{Mn}_{0.85}\text{PO}_4/\text{C}$ particles, and the formation of sufficient pores in the $\text{LiFe}_{0.15}\text{Mn}_{0.85}\text{PO}_4/\text{C}$ primary particles and aggregates. The facile and scalable solid-state reaction route proposed in the present study is of high efficiency and reliability, which is promising technique for massive production of high performance $\text{LiFe}_x\text{Mn}_{1-x}\text{PO}_4/\text{C}$ -based cathode material for high-energy density lithium ion batteries.

Acknowledgments

This work was supported by the special financial grant from the China Postdoctoral Science Foundation (2013T60795), the Guangzhou Scientific and Technological Planning Project (2013J4100112), the Guangdong Province Science & Technology Bureau (Industry-Education-Research Project, grant no. 2012B050300004), and the Fok Ying Tung Foundation (NRC07/08.EG01).

Appendix A. Supplementary data

Supplementary data related to this article can be found at <http://dx.doi.org/10.1016/j.jpowsour.2014.04.049>.

References

- [1] C. Masquelier, L. Crouguennec, Chem. Rev. 113 (2013) 6552–6591.
- [2] J.B. Goodenough, Y. Kim, Chem. Mater. 22 (2010) 587–603.
- [3] A.K. Padhi, K.S. Nanjundaswamy, J.B. Goodenough, J. Electrochem. Soc. 144 (1997) 1188–1194.
- [4] V. Aravindan, J. Gnanaraj, Y.S. Lee, S. Madhavi, J. Mater. Chem. A 1 (2013) 3518–3539.
- [5] D. Wang, H. Buqa, M. Crouzet, G. Deghenghi, T. Drezen, I. Exnar, N.H. Kwon, J.H. Miners, L. Poletto, M. Grätzel, J. Power Sources 189 (2009) 624–628.
- [6] D. Rangappa, K. Sone, Y. Zhou, T. Kudo, I. Honma, J. Mater. Chem. 21 (2011) 15813–15818.
- [7] M. Pivko, M. Bele, E. Tchernykhova, N.Z. Logar, R. Dominko, M. Gaberscek, Chem. Mater. 24 (2012) 1041–1047.
- [8] D. Choi, D.H. Wang, I.T. Bae, J. Xiao, Z.M. Nie, W. Wang, V.V. Viswanathan, Y.J. Lee, J.G. Zhang, G.L. Graff, Z.G. Yang, J. Liu, Nano Lett. 10 (2010) 2799–2806.
- [9] Z.H. Qin, X.F. Zhou, Y.G. Xia, C.L. Tang, Z.P. Liu, J. Mater. Chem. 22 (2012) 21144–21153.
- [10] X.H. Rui, X.X. Zhao, Z.Y. Lu, H.T. Tan, D.H. Sim, H.H. Hng, R. Yazami, T.M. Kim, Q.Y. Yan, ACS Nano 7 (2013) 5637–5646.
- [11] H. Yoo, M. Jo, B.S. Jin, H.S. Kim, J. Cho, Adv. Energy Mater. 1 (2011) 347–351.
- [12] Z. Bakenov, I. Taniguchi, Electrochim. Commun. 12 (2010) 75–78.
- [13] Z. Bakenov, I. Taniguchi, J. Power Sources 195 (2010) 7445–7451.
- [14] S.M. Oh, S.W. Oh, C.S. Yoon, B. Scrosati, K. Amine, Y.K. Sun, Adv. Funct. Mater. 20 (2010) 3360–3365.
- [15] S.M. Oh, S.W. Oh, S.T. Myung, S.M. Lee, Y.K. Sun, J. Alloys Compd. 506 (2010) 372–376.
- [16] P.R. Kumar, M. Venkateswarlu, M. Misra, A.K. Mohanty, N. Satyanarayana, J. Electrochem. Soc. 158 (2011) A227–A230.
- [17] B. Wang, D.L. Wang, Q.M. Wang, T.F. Liu, C.F. Guo, X.S. Zhao, J. Mater. Chem. A 1 (2013) 135–144.
- [18] S.K. Martha, J. Grinblat, O. Haik, E. Zinograd, T. Drezen, J.H. Miners, I. Exnar, A. Kay, B. Markovsky, D. Aurbach, Angew. Chem. Int. Ed. 48 (2009) 8559–8563.
- [19] H.L. Wang, Y. Yang, Y.Y. Liang, L.F. Cui, H.S. Casalongue, Y.G. Li, G.S. Hong, Y. Cui, H.J. Dai, Angew. Chem. Int. Ed. 50 (2011) 7364–7368.
- [20] L.J. Hu, B. Qiu, Y.G. Xia, Z.H. Qin, L.F. Qin, X.F. Zhou, Z.P. Liu, J. Power Sources 248 (2014) 246–252.
- [21] S.M. Oh, S.T. Myung, Y.S. Choi, K.H. Oh, Y.H. Oh, Y.K. Sun, J. Mater. Chem. 21 (2011) 19368–19374.
- [22] W. Liu, P. Gao, Y.Y. Mi, J.T. Chen, H.H. Zhou, X.X. Zhang, J. Mater. Chem. A 1 (2013) 2411–2417.
- [23] B. Ding, G. Ji, Y. Ma, P.F. Xiao, L. Lu, J.Y. Lee, J. Power Sources 247 (2014) 273–279.
- [24] K. Saravanan, V. Ramar, P. Balaya, J. Vittal, J. Mater. Chem. 21 (2011) 14925–14935.
- [25] G. Yang, H. Ni, H.D. Liu, P. Gao, H.M. Ji, S. Roy, J. Pinto, X.F. Jiang, J. Power Sources 196 (2011) 4747–4755.
- [26] S.M. Oh, H.G. Jung, C.S. Yoon, S.T. Myung, K. Amine, Y.K. Sun, J. Power Sources 196 (2011) 6924–6928.
- [27] Y.J. Zhong, J.T. Li, Z.G. Wu, X.D. Guo, B.H. Zhong, S.G. Sun, J. Power Sources 234 (2013) 217–222.
- [28] K. Zaghib, M. Trudeau, A. Guerfi, J. Trottier, A. Mauger, R. Veillette, C.M. Julien, J. Power Sources 204 (2012) 177–181.
- [29] S.M. Oh, S.T. Myung, J.B. Park, B. Scrosati, K. Amine, Y.K. Sun, Angew. Chem. Int. Ed. 51 (2012) 1853–1856.
- [30] S.M. Oh, Y.K. Sun, J. Power Sources 244 (2013) 663–667.
- [31] Z.Q. Huo, Y.T. Cui, D. Wang, Y. Dong, L. Chen, J. Power Sources 245 (2013) 331–336.
- [32] C. Hu, H. Yi, H. Fang, B. Yang, Y. Yao, W. Ma, Y. Dai, Electrochim. Commun. 12 (2010) 1784–1787.
- [33] J. Hong, F. Wang, X. Wang, J. Graetz, J. Power Sources 196 (2011) 3659–3663.
- [34] L.B. Ran, X.Y. Liu, Q.W. Tang, K.L. Zhu, J.H. Tian, J.Y. Du, Z.Q. Shan, Electrochim. Acta 114 (2013) 14–20.
- [35] A.Q. Pan, D. Choi, J.G. Zhang, S.Q. Liang, G.Z. Cao, Z.M. Nie, B.W. Arey, J. Liu, J. Power Sources 196 (2011) 3646–3649.
- [36] J.M. Kim, G.R. Yi, S.C. Lee, S.M. Lee, Y.H. Jo, H.W. Kang, G. Lee, H.J. Kim, J. Solid State Chem. 197 (2013) 53–59.
- [37] P.K. Harold, E.A. Leroy, X-ray Diffraction Procedure for Polycrystalline and Amorphous Materials, Wiley, New York, 1974.
- [38] C.M. Burba, R. Frech, J. Electrochem. Soc. 151 (2004) A1032–A1038.
- [39] M. Maccario, L. Crouguennec, B. Desbat, M. Couzi, F.L. Cras, L. Servant, J. Electrochim. Soc. 155 (2008) A879–A886.
- [40] Y. Bai, F. Wu, C. Wu, Chin. J. Light Scatt. 15 (2003) 231–236.
- [41] J.F. Qian, M. Zhou, Y.L. Cao, X.P. Ai, H.X. Yang, J. Phys. Chem. C 114 (2010) 3477–3482.
- [42] C.M. Julien, K. Zaghib, A. Mauger, M. Massot, M. Massot, A. Ait-Salah, M. Selmane, F. Gendron, J. Appl. Phys. 100 (2006) 063511.
- [43] A. Yamada, Y. Kudo, K.Y. Liu, J. Electrochim. Soc. 148 (2001) A747–A754.
- [44] H.S. Fang, Y.J. Hu, E.R. Dai, B. Yang, Y.C. Yao, W.H. Ma, Y.N. Dai, Electrochim. Acta 106 (2013) 215–218.
- [45] T. Liu, J.J. Xu, B.B. Wu, Q.B. Xia, X.D. Wu, RSC Adv. 3 (2013) 13337–13341.
- [46] J. Zong, Q.W. Peng, J.P. Yu, X.J. Liu, J. Power Sources 228 (2013) 214–219.
- [47] Y.F. Deng, Y.B. Zhou, Z.C. Shi, X. Zhou, X. Quan, G.H. Chen, J. Mater. Chem. A 1 (2013) 8170–8177.
- [48] R.V. Hagen, H. Lottmann, K.C. Moller, S. Mathur, Adv. Energy. Mater. 2 (2012) 553–559.
- [49] Z. Bakenov, I. Taniguchi, J. Electrochim. Soc. 157 (2010) A430.
- [50] L.L. Zhang, S. Duan, G. Peng, G. Liang, F. Zou, Y.H. Huang, J. Alloys Compd. 570 (2013) 61–64.